Generation of high-quality higher-order Laguerre–Gaussian beams using liquid-crystal-on-silicon spatial light modulators

Naoya Matsumoto,* Taro Ando, Takashi Inoue, Yoshiyuki Ohtake, Norihiro Fukuchi, and Tsutomu Hara

Central Research Laboratory, Hamamatsu Photonics K.K., Hirakuchi, Hamakita-ku, Hamamatsu-City 434-8601, Japan

**Corresponding author: nm@crl.hpk.co.jp*

Received March 14, 2008; revised May 2, 2008; accepted May 4, 2008; posted May 13, 2008 (Doc. ID 93896); published June 23, 2008

We report on the high-quality holographic generation of higher-order Laguerre–Gaussian (LG) beams using a liquid-crystal-on-silicon spatial light modulator. The effects of the input beam pattern on the output LG beam quality are investigated in detail through theoretical discussions and experiments. Correlation analyses between observed beam patterns and theoretical mode profiles reveal that higher beam quality is achieved for output LG beams generated from a top-hat input beam than from a Gaussian input beam. © 2008 Optical Society of America

OCIS codes: 090.1760, 100.5090, 120.5060, 140.3300, 230.3720.

1. INTRODUCTION

Laguerre–Gaussian (LG) beams were introduced as higher-order light modes in cylindrically symmetric optical cavities [1] and have been highlighted since Allen *et al.* [2] found that they carry angular momenta. So far, azimuthally higher- and radially lowest-order LG beams have been extensively studied [3–6] while radially higher-order LG beams have not attracted much attention [7–14]. However, radially higher-order LG beams, sometimes referred to as multiringed LG beams, are also interesting targets due to their properties that resemble Bessel beams and are expected to provide suitable tools for the manipulation of cold atoms [13,15]. Therefore it is meaningful to establish a systematical method for generating LG beams of both azimuthally and radially higher orders.

To establish a universal, flexible, and widely applicable scheme for generating higher-order LG beams, a holographic method using a spatial light phase modulator (SLM) is the most appropriate one because it also enables dynamical control of LG beam generation [5,16–19]. In a previous paper [20], Ohtake *et al.* reported the holographic generation of both azimuthally and radially higher-order LG beams using a liquid-crystal-on-silicon (LCOS) type SLM [21], which realizes programmable phase modulation with superior phase fidelity and diffraction efficiency. Multiringed LG beams can be holographically generated with phase patterns involving radial phase discontinuities; however, this is technically difficult, especially when the generating azimuthal and radial mode indices become larger. In this case, the holographic phase patterns involve more phase discontinuities to cause nonideal diffraction of light [22]. Moreover, phase distortion, which is inevitably included in the phase modulation characteristics of a liquid-crystal-on-silicon spatial light modulator (LCOS-SLM), deteriorates the quality of the holographically generated LG beams and decreases the trapping force in applications of atom manipulation [23]. Nevertheless, we achieved universal high-quality generation of higher-order LG beams using LCOS-SLM with compensation for phase distortion [20,21,23–26].

However, the effects of input beam patterns in holographic LG beam generation have not been highlighted so far. Ohtake *et al.* [20] reported on the universal generation of both azimuthally and radially higher-order LG beams using a top-hat input beam, while Gaussian input beams have been familiarly applied to LG beam generation through holographic conversion of the input beam [27]. In this paper, we further investigate the high-quality holographic generation of higher-order LG beams involving the effects of input beam patterns. In the present experiments, we adopted holographic phase patterns with partially added blazed phase grating patterns that were restricted to the central circular regions. This treatment enables a more precise boundary definition of the output beams and removal of the unmodulated components of the output beams, both of which help improve the output beam quality and facilitate quantitative experiments. As a semiquantitative benchmark of the output beam quality, we calculated the correlation coefficients between observed beam patterns and corresponding theoretical mode patterns. Experimental and theoretical comparisons were made between the output LG beams generated from the Gaussian and top-hat input beams to clarify that the top-hat input beam generates radially higher-order LG beams of higher quality than the Gaussian input beam.

This paper is organized as follows. In Section 2, we

describe the experimental aspects of the present study involving the characteristics of LCOS-SLM, the construction of the optical setup, and the holographic phase settings. Theoretical descriptions, experimental results, and discussions are presented in Section 3. Finally, this paper is closed with a summary and a conclusion in Section 4.

2. EXPERIMENTAL SETUP

In this paper, LG beams are holographically generated using a phase-only type LCOS-SLM [Hamamatsu X10468 series, whose active area consists of 792×600 pixels (pixel size, $20\ \mu m\times20\ \mu m$)]. This LCOS-SLM device is a reflective light phase modulation device equipped with a monolithic silicon circuit for electrically controlling the orientation of parallel-aligned nematic liquid crystal (LC) molecules. As a result, the LCOS-SLM device achieves easy and flexible use while special care is required in practical operations, particularly when precise phase setting is required. In the following, we describe the construction of experimental setups including a phase compensation method effective for generating high-quality LG beams [23].

A. Phase Modulation Device

1. Phase Modulation Characteristics

Figure 1 shows a schematic displaying the structure of the LCOS-SLM device. An LC layer is sandwiched between a pair of alignment layers and attached to an optically flat glass substrate (thickness, 3 mm) via a transparent electrode layer. A silicon backplane, equipped with an active matrix circuit directly connected to the pixelated metal electrodes, is mounted onto the other side of the LC layer to control the orientation of the LC molecules at each pixel. In the following, we refer to the pixel placed at the horizontally xth and vertically yth position as simply the (x,y) pixel.

Note that the silicon backplane can be mechanically distorted during the fabrication process because the silicon substrate is not sufficiently thick to maintain flatness against the mechanical tension. Hence the LC layer, which lies between the flat glass substrate and the distorted silicon backplane, is distributed nonuniformly over the device surface to cause position-dependent phase modulation characteristics that are classified into two types: The position-dependent response of the phase modulation value to the control voltage and the position-dependent phase offset at zero control voltage. Here, from

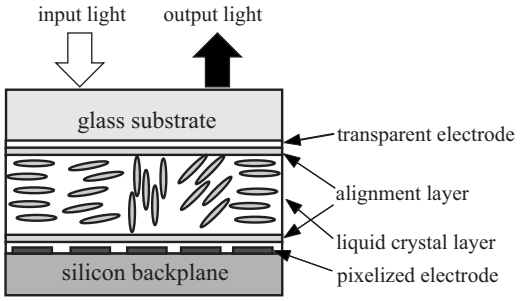

Fig. 1. Structure of the LCOS-SLM device, cross-sectional picture.

the fact that the amount of phase modulation is proportional to the optical path length through which an incident light passes, the response of the phase modulation value to the control voltage can be decomposed to a product of the electric response of the LC material [$n(V)$ with V as the control voltage] and the thickness of the LC layer at (x,y) pixel ($d_{x,y}$). Thus the total position-dependent inhomogeneous phase modulation ($\phi_{x,y}$) can be expressed as follows:

$$\phi_{x,y}(V)=\Delta\phi_{x,y}(V)+\phi_{x,y}(0)=n(V)d_{x,y}+\phi_{x,y}^{\mathrm{fix}},\qquad(1)$$

where the modulation term $\Delta\phi_{x,y}(V)=\phi_{x,y}(V)-\phi_{x,y}(0)$ depends on both the pixel position and the control voltage, while $\phi_{x,y}(0)=\phi_{x,y}^{\mathrm{fix}}$ is a constant offset term given at each pixel position; $\Delta\phi_{x,y}(V)$ and $\phi_{x,y}(0)$ are independently distorted, and separate measurements are required to clarify both terms.

2. Compensation Procedure for Inhomogeneous Phase Modulation

To realize precise phase modulation with LCOS-SLM, the inhomogeneous phase modulation characteristics described in Eq. (1) must be compensated for. In the following, we briefly summarize the phase compensation scheme, which plays a principal role in holographic mode generation using LCOS-SLM. A more detailed explanation involving information of the device operation can be found in [21].

The first step of the phase compensation scheme is the measurement of the actual amount of the phase modulation with respect to the change of the control voltage. In general, phase distribution can be measured using a Michelson interferometer (MIF) setup with replacing one of the mirrors to LCOS-SLM. However, this approach derives total phase modulation, i.e., $\phi_{x,y}(V)$. To separately measure $\Delta\phi_{x,y}(V)$, we can apply a polarization interferometer (PIF) setup because LCOS-SLM only modulates the phase of the linearly polarized component in the alignment direction of the LC molecules.

Applying the above measurement method for the phase modulation characteristics, phase compensation is performed as follows.

Step 1. Measure $\Delta\phi_{x,y}(V)$ at each pixel of LCOS-SLM by PIF with varying V.

Step 2. Make look up tables (LUTs) between the actual phase modulation values and the control voltages to establish their correspondence. We use a common LUT for a block of pixels that contains 6×6 neighboring pixels, which present similar characteristics.

Step 3. Display a uniform phase image on the LCOS-SLM device with the help of the LUTs obtained in Step 2 and measure the output wavefront with MIF. The obtained phase distribution corresponds to $\phi_{x,y}(0)$.

Step 4. Calculate the control voltages for canceling $\phi_{x,y}(0)$, which give the offset values of the control voltages.

Practically, the control voltage is discretized into 256 steps, where values 0 and 255 correspond to the phase values of 0 and 2π, respectively. Moreover, the phase measurement in Step 1 requires a light from a xenon lamp

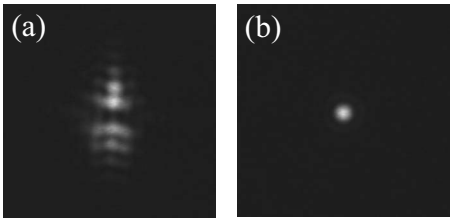

Fig. 2. Focal patterns of the top-hat incident beam reflected on the LCOS-SLM device (a) without and (b) with the phase compensation.

through an interference filter to avoid a speckle noise. By adding the offset pattern obtained in Step 4, we can correctly display the desired phase patterns on LCOS-SLM.

3. Effects of Phase Compensation

Following the procedure in Subsection 2.A.2, we can realize a nearly ideal light phase modulation with LCOS-SLM. Figure 2 displays the focal patterns of a top-hat beam through the LCOS-SLM with and without phase compensation. Here, even though the LCOS-SLM is set to act as a flat mirror, the output beam is blurred due to phase distortion without the compensation as seen in Fig. 2(a). On the other hand, Fig. 2(b) shows that the compensation prominently improves the phase distortion so that the focal pattern is close to the ideal Airy disk.

We note that the above phase compensation procedure compensates for the phase distortion attached to the light on LCOS-SLM. However, another phase distortion can be introduced by the misalignment of optical elements in the experimental setup. In Subsection 2.B, we present in detail the practical setup for generating and observing high-quality LG beams.

B. Optical Setup

1. Construction of Optical Systems

Practically, an input light pattern influences the output mode purity in the holographic generation of LG beams. So far, Gaussian input beams have generally been applied to obtain LG beams [5–7,11,28]. However, there are no quantitative studies on the effects of incident light patterns to the output mode purity in the generation of both azimuthally and radially higher-order LG beams. In this

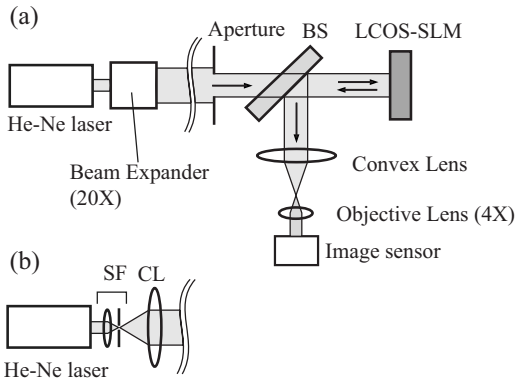

Fig. 3. Schematic of experimental setups. (a) Setup for a Gaussian input beam and (b) setup for a top-hat input beam. BS, SF, and CL indicate beam splitter, spatial filter, and collimation lens, respectively.

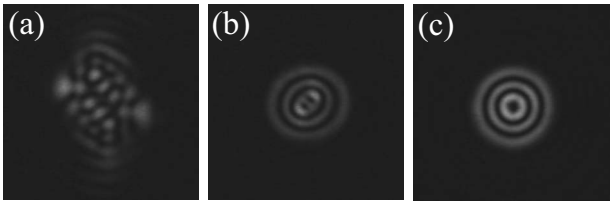

Fig. 4. Observed mode patterns of the LG_2^1 beam. (a) Without any compensations, (b) with a compensation only for phase distortion of the LCOS-SLM, and (c) with careful adjustment of the tilt of the lens.

paper, we compare the output mode patterns for Gaussian and top-hat input lights to investigate the effects of input light patterns.

Figure 3 shows a schematic of the experimental setups. An input light, either Gaussian or top-hat, is projected onto the LCOS-SLM, where the light is attached to a phase distribution of a required LG mode. The output light, which propagates in a slightly different direction to the unmodulated zeroth-order output light due to the blazed phase pattern, is extracted by the beam splitter (BS) placed in front of the LCOS-SLM, modified through the combination of a convex lens ($f=400$ mm) and an objective lens ($4\times$), and detected with an image sensor (we used a CCD camera as the image sensor in this paper). Choosing either the optical setups of Fig. 3(a) or 3(b), we can perform experiments with top-hat and Gaussian input lights, respectively. Here, the aperture in Fig. 3 restricts the irradiation range to avoid diffraction from the edges of the LCOS-SLM device. In this paper, we apply an alternate approach to strictly define the boundary of the incident and output lights (see Subsection 2.B.2).

In addition to the precision of the holographic phase pattern, aberration in the optical system obstructs the precise evaluation of the output LG beam quality [23]. Figure 4 demonstrates the effects of the phase compensation and aberration on the holographic generation of the LG_2^1 beam under the existence of the lens tilt. The output LG_2^1 beam, which is far from an ideal mode pattern without phase compensation and aberration correction [Fig. 4(a)], is improved by phase compensation [Fig. 4(b)], but the mode pattern includes the effect of the lens tilt to present a figure that resembles the patterns shown in [14]. The aberration due to the lens tilt is removed in Fig. 4(c) by careful optical adjustment.

2. Phase Settings

To determine the phase patterns for generating LG beams, the phase structures of the desired LG beams are required. We start from an electric field amplitude u_p^l of the LG_p^l beam based on the paraxial and scalar wave approximations. Supposing that the LG_p^l beam propagates in the z direction and is focused at $z=0$, u_p^l is expressed as the following with respect to cylindrical coordinates (r,ϕ,z) [2]:

$$u_p^l(r,\phi,z) = (-1)^p \left[\frac{2}{\pi}\frac{p!}{(p+|l|)!}\right]^{1/2} \frac{(\sqrt{2}\xi)^{|l|}}{w_z} \exp(-\xi^2) \times L_p^{|l|}(2\xi^2)\exp(-il\phi)\exp(-i\xi^2 z/z_R) \times \exp[i(2p+|l|+1)\tan^{-1}(z/z_R)], \quad (2)$$

where $L_p^{|l|}(x)$ denotes a generalized Laguerre polynomial (strictly, this should be referred to as a Sonine polynomial). In Eq. (2), z_R and $w_z\{=[2(z^2+z_R^2)/(kz_R)]^{1/2}\}$ indicate a Rayleigh length and beam radius at z, respectively, with k as a wavenumber of the incident light. Additionally, a scaled radial variable $\xi=r/w_z$ is also introduced in the above expression for simplicity.

A cross-sectional phase structure of the LG_p^l beam is determined by the azimuthal phase terms $\exp(-il\phi)$ and $L_p^{|l|}(2\xi^2)$. $L_p^{|l|}(x)$ alternately changes its sign as x passes over p different zero points of the Laguerre polynomial; hence the phase structure has π phase discontinuities at every node in the radial direction. In combination with the helical phase structure determined by the term $\exp(-il\phi)$, the total phase pattern for converting the plane-wave input lights to the LG_p^l beam is given as

$$\varphi(r,\phi) = -l\phi + \pi\theta(-L_p^{|l|}(2r^2/w_0^2)) \tag{3}$$

with $\theta(x)$ as a unit step function. When displayed on LCOS-SLM, the phase value is wrapped in the interval between 0 and 2π.

Figure 5 demonstrates the phase patterns for generating LG_3^3 and LG_5^5. Practically, output lights from LCOS-SLM include unmodulated components. These unmodulated components, which deteriorate the output beam quality, are separated from the desired output beam by adding a blazed phase grating pattern to such phase patterns as in Fig. 5. Moreover, the blazed phase pattern is restricted to the circular area at the center of the phase pattern. This treatment plays the role of realizing a programmable aperture, which can define the boundary of the output light patterns more precisely than the mechanical aperture. Figure 6 exhibits the phase patterns for generating the LG_3^3 and LG_5^5 beams that were actually used in the experiments.

As described above, the blazed phase pattern diffracts an output beam into a different direction to a zeroth-order beam that propagates in the normal direction to the SLM surface. Resultantly, the output beams are scaled down in the diffraction direction (horizontal direction for the phase patterns as in Fig. 6) when observed from the first-order diffraction direction. However, the angle between the zeroth- and first-order diffraction directions is at most 0.226 rad in our experiments, and the output beams are scaled down by less than ~0.0016%, which produces no observable effects.

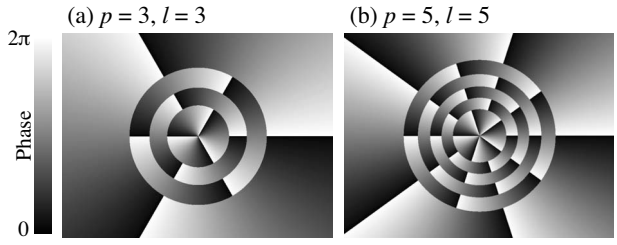

Fig. 5. Examples of phase pattern for generating (a) LG_3^3 and (b) LG_5^5 beams.

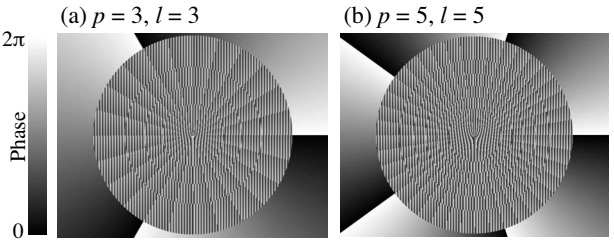

Fig. 6. Phase patterns obtained by adding blazed phase grating patterns to those shown in Fig. 5 for (a) LG_3^3 and (b) LG_5^5.

3. RESULTS AND DISCUSSIONS

A. Theoretical Description

1. Analysis of Mode Pattern

In this paper, an observed light pattern is analyzed in comparison to a corresponding theoretical LG mode pattern $I_p^l(r,\phi,z)$, where both observed and theoretical patterns are treated as two-dimensional,

$$I_p^l(r,\phi,z) = |u_p^l(r,\phi,z)|^2 = \frac{2}{\pi w_z^2}\frac{p!}{(p+|l|)!}\left(2\frac{r^2}{w_z^2}\right)^{|l|} \times \exp\left(-2\frac{r^2}{w_z^2}\right)\left[L_p^{|l|}\left(2\frac{r^2}{w_z^2}\right)\right]^2. \tag{4}$$

We notice from Eq. (4) that I_p^l is independent of ϕ and that its cross section presents a similar figure at every z position. The theoretical mode pattern should be expressed in the two-dimensional Cartesian coordinates on the image plane for fitting the observed pattern to the theoretical one because the output beams are observed with a CCD camera to provide data as two-dimensional arrays. Moreover, experimentally obtained beam patterns usually include background noises. Thus we adopt the following model function for the fitting analysis of the observed beam pattern:

$$I_p^l(x,y;B_0,C_0,w_z) = B_0 + C_0\frac{2}{\pi w_z^2}\frac{p!}{(p+|l|)!}\left(2\frac{x^2+y^2}{w_z^2}\right)^{|l|} \times \exp\left(-2\frac{x^2+y^2}{w_z^2}\right)\left[L_p^{|l|}\left(2\frac{x^2+y^2}{w_z^2}\right)\right]^2, \tag{5}$$

where B_0 and C_0 are the offset due to the background noise and scaling factor corresponding to the total output light power, respectively. In Eq. (5), the center position of the observed beam pattern is omitted for notational simplicity, but explicit dependency on the center position can be retrieved by applying the substitution of $x\rightarrow(x-O_x)$ and $y\rightarrow(y-O_y)$ with O_x and O_y as the x and y directional positions of the beam center.

In practical analysis, we first calculate the centroid of the observed mode pattern and extract partial data at 280×280 pixels around the centroids to avoid analyzing meaningless data. The fitting analysis is performed between the extracted pattern and the two-dimensional model function [Eq. (5)] with choosing (C_0,w_z,O_x,O_y) as fitting parameters while B_0 is fixed to an average value of the data removed from the original pattern. With the values of the fitting parameters that minimize the sum of the

squared residuals between the model and the observed pattern, we calculate the correlation coefficient between them to semiquantitatively estimate the mode purity.

We note that the analyses are performed for two-dimensional beam patterns while previous papers presented quantitative discussions based on one-dimensional analyses for cross-sectional mode profiles [11,13,28]. The two-dimensional analysis adopted in this paper enables direct comparisons between the theoretical models and the observed patterns without the artificial treatment of the data, although much computational cost is required. Additionally, a two-dimensional analysis can correctly evaluate the deformation of the output beam patterns as a deterioration of beam quality even when they become asymmetric under the presence of the lens tilt.

2. Mode Purity

We can estimate the output mode purity that can be achieved with the present generation scheme by analyzing the electric field amplitude of light on the LCOS-SLM surface. In the following, we derive an explicit expression of mode purity to show that maximum mode purity is achieved by adjusting the sizes of phase patterns relative to incident light size.

Complex amplitude c_q^k of the LG_q^k content in the output light is calculated as an inner product of the analytic signal of the output light and that of the LG_q^k mode [11,28]. In this paper, we only consider the output beam of the first-order diffraction for simplicity and omit the reflection function due to the blazed phase pattern from the following expressions.

We start from the assumption that an incident light has a flat wavefront at the LCOS-SLM surface, i.e., the LCOS-SLM surface corresponds to $z=0$. The analytic signal of the output beam on the LCOS-SLM surface is proportional to $A(r)\Psi_p^l(r,\phi)$ with amplitude factor $A(r)$ and phase factor $\Psi_p^l(r,\phi)$ defined as

$$A(r)=\begin{cases}\theta(R_0-r) & \text{top-hat}\\ \exp\left(-\dfrac{r^2}{w_i^2}\right)\theta(R_0-r) & \text{Gaussian}\end{cases}, \tag{6}$$

(w_i denotes the radius where the light power becomes $1/e^2$ of that at the center for a Gaussian input beam) and

$$\Psi_p^l(r,\phi)=\exp[-i\varphi(r,\phi)]=\exp(-il\phi)[2\theta(L_p^{|l|}(2r^2/w_0^2))-1], \tag{7}$$

respectively. Here Eq. (7) is derived with the help of Eq. (3) and $\exp[i\pi\theta(-x)]=2\theta(x)-1$. Since the blazed phase pattern is limited to the circular regime of radius R_0 (see Fig. 6, $R_0=290$ pixels in our experiments), Eq. (6) contains step functions to restrict the amplitude distributions.

When LCOS-SLM displays the phase pattern for generating the LG_p^l beam, c_q^k is expressed as

$$c_q^k=A_0\int_0^{2\pi}\mathrm{d}\phi\int_0^{\infty}r\mathrm{d}r\,A(r)\Psi_p^l(r,\phi)u_q^k(r,\phi,0)^*, \tag{8}$$

where * denotes the complex conjugate and A_0 is a normalization factor for $A(r)$ defined as

$$A_0=\left[\int_0^{2\pi}\mathrm{d}\phi\int_0^{\infty}r\mathrm{d}r\,A(r)^2\right]^{-1/2}=\begin{cases}\dfrac{1}{\sqrt{\pi}R_0} & \text{top-hat}\\ \dfrac{1}{\sqrt{\pi}w_i}\left[\dfrac{2}{1-\exp(-2R_0^2/w_i^2)}\right]^{1/2} & \text{Gaussian}\end{cases}. \tag{9}$$

Performing the ϕ integration in Eq. (8), we find that c_q^k becomes nonzero only when $k=l$. Thus, Eq. (8) is reduced to the following form:

$$c_q^l(a)=\left[\frac{q!}{(q+|l|)!}\right]^{1/2}\frac{(-1)^qR_0A_0}{\sqrt{\pi}2^{3/2}a}\times\int_0^{2a^2}\mathrm{d}\zeta\,\zeta^{|l|/2}L_q^{|l|}(\zeta)[2\theta(L_p^{|l|}(\zeta))-1]\times\begin{cases}\exp(-\zeta/2) & \text{top-hat}\\ \exp\left[-\left(1+\dfrac{R_0^2}{w_i^2}\dfrac{1}{a^2}\right)\dfrac{\zeta}{2}\right] & \text{Gaussian}\end{cases}, \tag{10}$$

where $a=R_0/w_0$ with w_0 as a beam radius of the output beam on the SLM surface and $\zeta=2r^2/w_0^2$. In the case of $p=q$, Eq. (10) is further simplified using $L_p^{|l|}(x)[2\theta(L_p^{|l|}(x))-1]=|L_p^{|l|}(x)|$.

The output mode content η of the desired mode is given by $\eta=|c_p^l|^2$ as a function of a. Figures 7 and 8 show the changes of η with varying a for Gaussian and top-hat input beams, respectively. To study the behavior of η for different p and l, η was calculated for different p with the

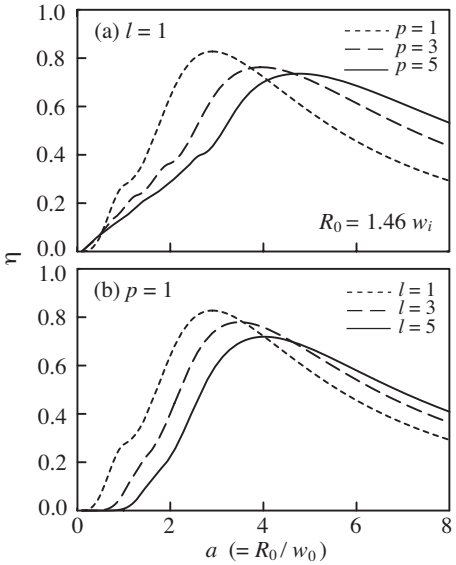

Fig. 7. Theoretical output mode purities as functions of a for Gaussian-beam input under the condition of $R_0=1.46\,w_i$. (a) In the case of fixed l ($l=1$), dotted, dashed, and solid curves are mode purities for $p=1$, 3, and 5, respectively. (b) In the case of fixed p ($p=1$), dotted, dashed, and solid curves are mode purities for $l=1$, 3, and 5, respectively.

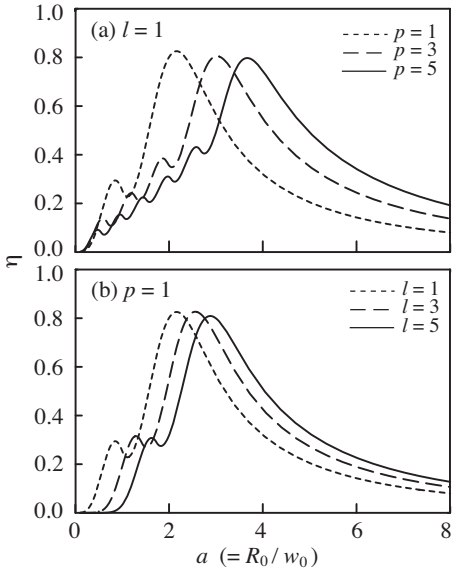

Fig. 8. Theoretical output mode purities as functions of a for top-hat beam input. (a) In the case of fixed l ($l=1$), dotted, dashed, and solid curves are mode purities for $p=1$, 3, and 5, respectively. (b) In the case of fixed p ($p=1$), dotted, dashed, and solid curves are mode purities for $l=1$, 3, and 5, respectively.

same l (=1) and for different l with the same p (=1). We notice in Figs. 7 and 8 that η exhibits a maximum $\eta_{\max}$ at a particular $a_{\max}$ depending on p and l and that $a_{\max}$ increases as the mode indices (p,l) become larger. According to this fact, we can maximize the output LG mode purity by choosing $w_0=290/a_{\max}$ pixel when displaying the phase pattern [Eq. (3)] on LCOS-SLM. However, $\eta_{\max}$ monotonously decreases as the radial and/or azimuthal order of the target LG mode becomes higher (note that we chose $R_0=290$ pixels in Subsection 3.A.2). The effects of the input light pattern are observed as follows: η is not so sensitive to the change of a, but the decrease of $\eta_{\max}$ for higher modes is significant for Gaussian input light while η is sensitive to the change of a, but the decrease of $\eta_{\max}$ for higher modes is slight in the case of top-hat input light. This tendency is also seen for even larger p and l. Therefore, we expect that a top-hat input light has an advantage over a Gaussian input light in generating LG beams of both radially and azimuthally higher orders.

As seen in Eq. (10), the choice of w_i also influences the output mode purity in the case of the Gaussian input beam. However, the choice of extremely large or small w_i should be avoided because the input Gaussian beam approaches the top-hat pattern to lose the Gaussian characteristics for large w_i, whereas the phase structure for maximizing the mode purity becomes extremely fine for small w_i. In this paper, we chose $w_i=198$ pixels on the LCOS-SLM surface, a value that realizes an input pattern sufficiently different from the top-hat pattern and keeps the required holographic phase pattern practically available.

Note that c_p^l is conserved during the propagation of the output beam for each mode content and that η at the observing plane is identical to that at the LCOS-SLM surface. Thus the above discussion is valid to analyze the mode purities of the observed mode patterns.

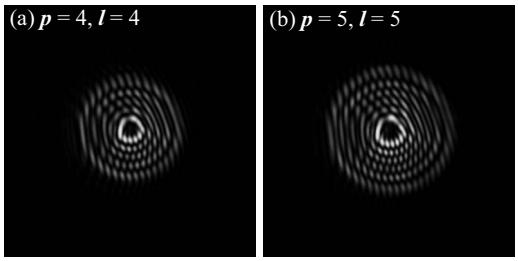

Fig. 9. Interference patterns of generated beams and the plane reference waves for (a) LG_4^4 and (b) LG_5^5 generated from a top-hat input beam.

B. Experimental Results

1. Phase Structures of Observed Beams

Prior to the investigation of beam patterns, we confirmed the phase structures of the generated beams through observing the interference patterns of output beams and the plane reference wave with a Mach–Zehnder interferometer. Figure 9 displays typical interference patterns of the output beams generated using a top-hat input beam through the holographic phase patterns of LG_4^4 and LG_5^5 modes, respectively. In Fig. 9, we can observe forklike phase branches corresponding to azimuthal mode index $|l|$ of the observed beams as well as radial phase discontinuities corresponding to radial mode index p, which reflect the phase properties of LG beams. Similar interference patterns were also observed for other output beams and those generated from a Gaussian input beam, suggesting that all output beams in this paper are indeed of LG beams from the phase structures and the observed beam patterns shown in Subsections 3.B.2 and 3.B.3.

2. Gaussian Input Beam

In this section, we show the experimental results with a Gaussian input beam obtained using the experimental setup in Fig. 3(a). Figure 10 shows the observed beam patterns of the multiringed LG_p^l $(p,l=1,2,3)$ beams. The drawing region is 280×280 pixels around the centroid of each beam pattern, the region in which the fitting analysis was performed. The symmetrical shapes of the observed beam patterns confirm that aberration of the optical system is sufficiently removed to study the output beam quality.

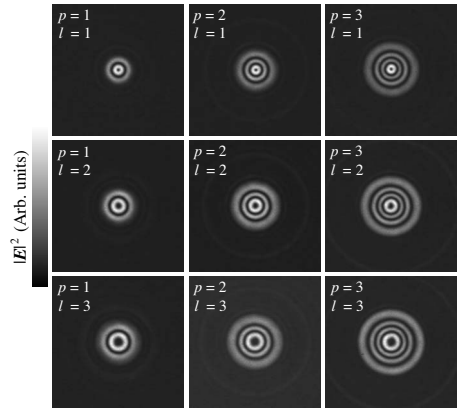

Fig. 10. Observed beam patterns of LG_p^l $(p,l=1,2,3)$ beams generated from Gaussian input beams.

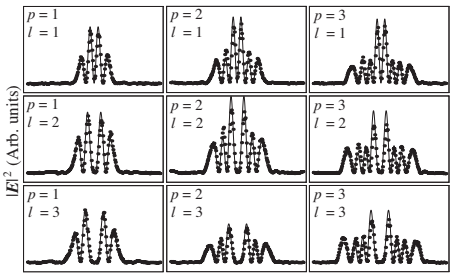

Fig. 11. Cross sections of observed mode patterns (closed circles) with corresponding fitted profiles (solid curves) for LG_p^l modes of $p,l=1,2,3$. Results are aligned corresponding to Fig. 10.

Figure 11 displays cross sections of the observed beam patterns (closed circles) and fitted profiles (solid curves) corresponding to the beam patterns in Fig. 10. Here we again stress that fitting calculations are performed for two-dimensional profiles and that Fig. 11 only exhibits part of the total information for demonstrative purposes.

Figure 12 demonstrates the observed beam patterns of further higher-order multiringed LG beams, e.g., LG_5^1, LG_1^5, LG_5^5, and LG_1^7 beams. Cross-sectional profiles and fitted curves are shown in Fig. 13. We notice in Fig. 13 that the observed patterns present the overall correspondence with the fitted profiles; however differences between the observed beam profiles and the theoretical ones are notable at the outermost sidelobes. This deviation at the outermost sidelobe appears to be a common property of radially higher-order LG beams generated from the Gaussian input beam.

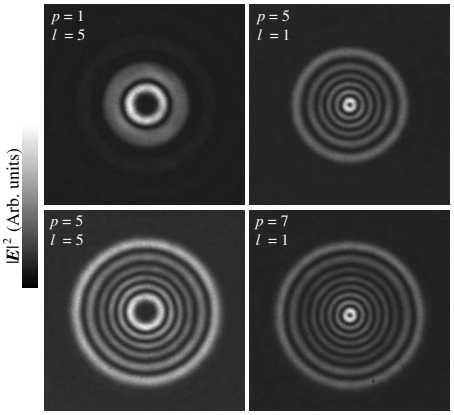

Fig. 12. Observed beam patterns of higher-order LG beams generated from a Gaussian input beam.

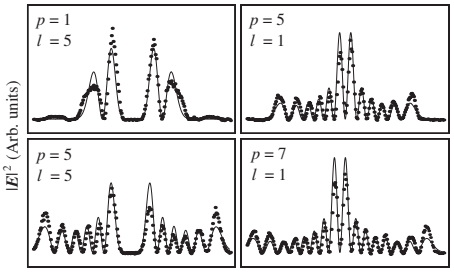

Fig. 13. Cross sections of observed beam patterns (closed circles) with the corresponding fitted profiles (solid curves) for further higher-order LG beams. Results are aligned corresponding to Fig. 12.

We note that the observed beam pattern is a Fourier transformed one magnified through an objective lens (Fig. 3); hence a radius of observed beam w_z, which is determined by a fitting calculation of the observed pattern, is proportional to $a=R_0/w_0$. As mentioned in Subsection 3.A.2, the size of a holographic phase pattern is determined with respect to a so that the output beam purity is maximized for each beam. With properly scaling the values of a and w_z, we confirmed correspondence of w_z to a for each LG_p^l beam with a deviation of less than 7.5%. Additionally, asymptotic standard errors of w_z derived from the fitting analyses were less than 0.021% for all the observed beams, indicating confidence of the analyses.

3. Top-Hat Input Beam

In this section, we present experimental results obtained with a top-hat input beam for comparison with the results obtained from a Gaussian input beam. Figure 14 shows the observed mode patterns of multiringed LG_p^l $(p,l=1,2,3)$ beams generated from the top-hat input beam. Additionally, Fig. 15 demonstrates cross sections of the observed mode patterns (closed circles) and fitted profiles (solid curves) corresponding to Fig. 14.

Figures 16 and 17, respectively, show the observed beam patterns and the corresponding cross-sectional profiles with fitted curves of further higher-order LG beams, e.g., LG_5^1, LG_1^5, LG_5^5, and LG_1^7, generated from the top-hat input beam. We also observe agreement between the cross-sectional beam patterns and the fitted profiles, also

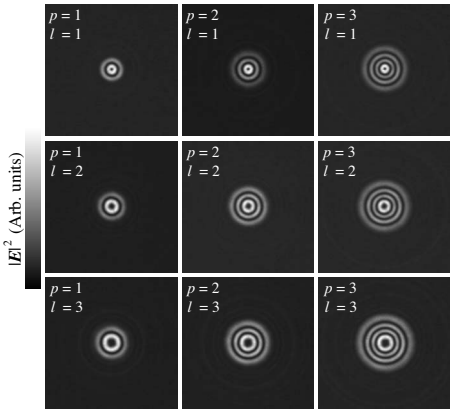

Fig. 14. Observed mode patterns of LG_p^l $(p,l=1,2,3)$ beams generated from a top-hat input beam.

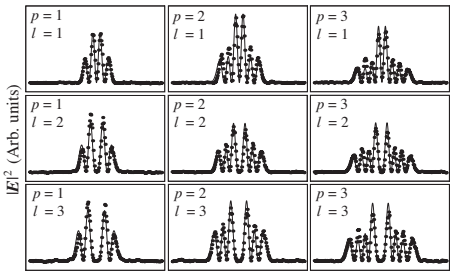

Fig. 15. Cross sections of observed mode patterns (closed circles) with the corresponding fitted profiles (solid curves) for LG_p^l modes of $p,l=1,2,3$. Results are aligned corresponding to Fig. 14.

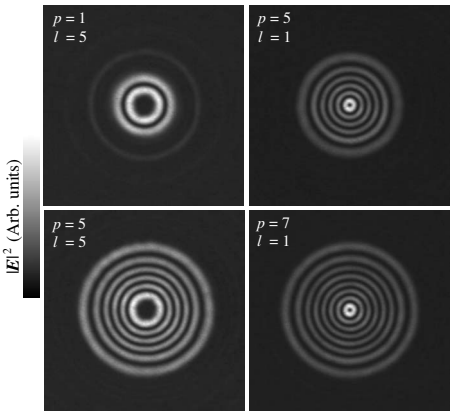

Fig. 16. Observed mode patterns of higher-order LG beams generated from a top-hat input beam.

at the outermost sidelobes, indicating that the top-hat input beam is suitable for generating a higher-order LG beam.

The behavior of w_z with respect to a was also confirmed as in the case of Gaussian input. As a result, w_z corresponds to properly scaled a for each LG_p^l beam with a deviation of less than 4.7%, suggesting that the present LG beam generation involves fewer extrinsic effects. Asymptotic standard errors of w_z derived from the fitting analyses were less than 0.025%, again indicating confidence of the analyses.

C. Discussion

We start a discussion from the mode purity of the output beams in the generation of higher-order LG beams. As described in Subsection 3.A.2, the output beams generally contain the mode contents of various radial mode index p. Table 1 displays the mode contents of the LG_0^1 beam theoretically evaluated by assuming Gaussian and top-hat input beams. Two significant facts in Table 1 are also true for other radially lowest-order LG modes: The Gaussian input beam is more suitable for high-quality generation of radially lowest-order LG beams, and the dominant mode contents of the output beam are localized to the ten lowest-order components. Based on this fact, previous reports practically performed quantitative analyses of mode purity by decomposing output beams as sums of the mode contents of various p [11].

Contrarily, the situation is different for radially higher-order LG beams. As an example, Table 2 demonstrates the theoretically derived lowest 30 mode contents of the

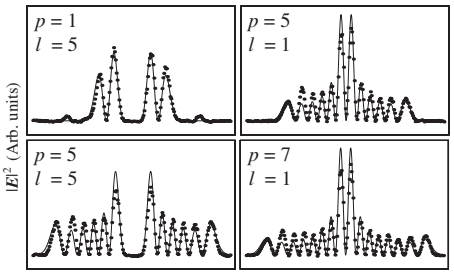

Fig. 17. Cross sections of observed mode patterns (closed circles) with the corresponding fitted profiles (solid curves) for further higher-order LG beams. Results are aligned corresponding to Fig. 16.

Table 1. Mode Contents of the First Ten Components of the Holographically Generated $LG_{p=0}^{l=1}$ Beam

	Mode Contents	
p	Gaussian Input	Top-Hat Input
0	9.35×10^{-1}	8.66×10^{-1}
1	2.96×10^{-14}	1.04×10^{-14}
2	1.75×10^{-2}	2.33×10^{-2}
3	1.93×10^{-2}	3.71×10^{-6}
4	3.54×10^{-3}	1.83×10^{-2}
5	9.12×10^{-4}	2.45×10^{-2}
6	2.24×10^{-3}	9.54×10^{-3}
7	3.93×10^{-3}	3.59×10^{-4}
8	3.06×10^{-3}	1.31×10^{-3}
9	1.22×10^{-3}	2.70×10^{-3}
Sum	0.987	0.946

LG_3^1 beam generated from a top-hat input beam. The significant mode contents are widely distributed, and the total of the mode contents becomes at most 0.925 up to the order of $p=29$, which is far from unity. These widely distributed mode contents are commonly observed in the generation of radially higher-order LG beams regardless of whether the input beam is Gaussian or top-hat. Mode decomposition analysis including a large amount of mode content is computationally unstable and fails even if a computer with sufficient resources is provided, indicating that mode decomposition analysis is practically ineffective for holographically generated radially higher-order LG beams. Therefore, correlation analysis between observed and fitted mode patterns is the only approach presently available.

Figure 18 shows correlation coefficients R and theoretical mode purities η of holographically generated LG beams, which are obtained through fitting analyses of observed beam patterns described in Subsections 3.B.2 and 3.B.3. In Fig. 18, both R and η show a tendency to decrease as the mode indices of the generated LG beam become larger, but the decrease is slighter for LG beams generated from a top-hat input beam. However, further

Table 2. First 30 Mode Contents of the Holographically Generated $LG_{p=3}^{l=1}$ from a Top-Hat Input Beam

	p (Figure of the First Place)		
$*$	$0*$	$1*$	$2*$
0	6.05×10^{-4}	2.84×10^{-3}	1.20×10^{-3}
1	5.83×10^{-3}	3.15×10^{-3}	7.95×10^{-4}
2	8.16×10^{-3}	1.11×10^{-2}	7.60×10^{-4}
3	8.05×10^{-1}	2.13×10^{-3}	4.54×10^{-4}
4	4.89×10^{-3}	2.01×10^{-3}	3.30×10^{-6}
5	7.00×10^{-3}	6.75×10^{-3}	1.69×10^{-3}
6	1.92×10^{-4}	2.63×10^{-3}	6.87×10^{-3}
7	9.97×10^{-3}	1.86×10^{-5}	1.19×10^{-2}
8	1.91×10^{-3}	1.60×10^{-3}	1.17×10^{-2}
9	5.04×10^{-3}	1.99×10^{-3}	6.48×10^{-3}
Sum			0.925

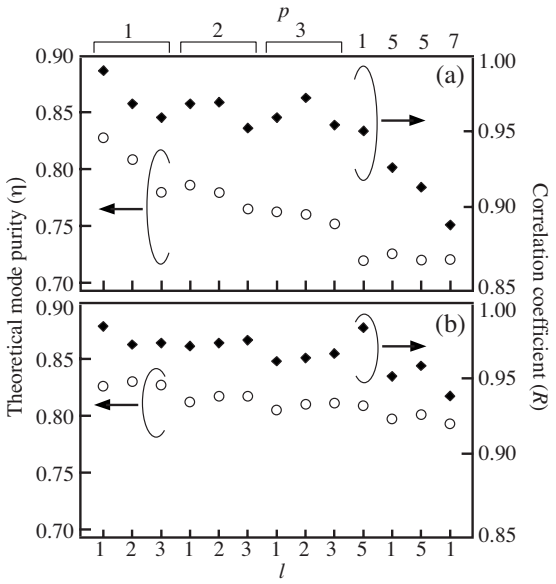

Fig. 18. Correlation coefficient R and mode purity η of holographically generated LG_p^l beams from (a) Gaussian and (b) top-hat input beams.

discussion on the relationship between R and η should be required to conclude from experimentally obtained R that the top-hat input beam can generate higher-order LG beams with higher quality than the Gaussian input beam.

Strictly, correlation coefficient R is not a quantitative benchmark of η, e.g., we should also keep in mind that R generally varies during beam propagation while η does not and that R suffers from residual aberrations in a practical optical setup. To investigate the relation between R and η, R is plotted as a function of η in Fig. 19. We observe in Fig. 19 a globally monotonous increase of R according to η, although a clear linear relation is not seen. From this result, R is considered to involve sufficiently fewer extrinsic effects to provide a relative benchmark of η at least for LG beam patterns observed under a same experimental condition.

Based on the above discussion on R and η with Figs. 18 and 19, we proceed to the discussion of the effects of the input beam pattern on the holographic generation of LG beams. At first, R and η are similar for Gaussian and top-hat input conditions when generating LG beams of $p=1$. This result leads to both Gaussian and top-hat input beams producing LG beams of similar quality for lower-order modes. For LG_p^l beams of $p \geq 2$, η gives a smaller value for the Gaussian input condition even though R is similar for both conditions, meaning that a mode-purity estimation by R tends to overestimate η of LG beams generated from a Gaussian input beam. Nevertheless, for LG_p^l beams of p or $l>3$, the Gaussian input condition presents smaller R values than the top-hat input condition, clearly suggesting the advantage of the top-hat input condition for achieving larger η. Consequently, we can conclude the superiority of the top-hat input beam in the holographic generation of LG beams particularly for generating higher-order LG_p^l beams of p or $l>3$.

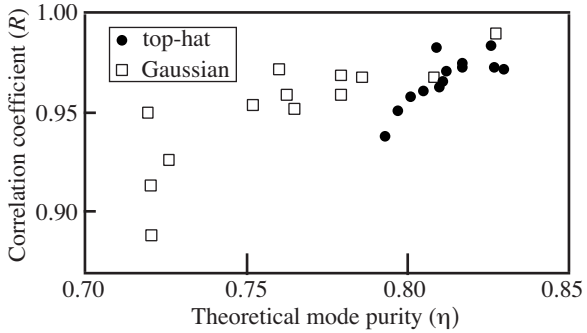

Fig. 19. Plot of correlation coefficient R as a function of theoretical mode purity η. Closed circles indicate values derived from the results of top-hat input while open squares indicate those from the results of Gaussian input.

Although we established the role of R as an experimental benchmark of output LG beam purity η, deviations still remain between R and η in Fig. 19. We consider the deviation to be caused by the nonideal behavior of LCOS-SLM, e.g., effects of nonideal phase profiles at the rapid phase changes (usually referred to as the "flyback region" [22]), pixelized electrode structure, and stepwise phase setting of the LCOS-SLM device. Further investigation is required to confirm the effects of these extrinsic factors on the holographic generation of LG beams.

4. SUMMARY AND CONCLUSION

This paper examined the generation of high-quality higher-order LG beams. To display holographic phase patterns on LCOS-SLM with sufficient fidelity, we introduced phase compensation for the position-dependent inhomogeneous phase modulation characteristics of LCOS-SLM. Moreover, by adding blazed phase grating patterns restricted to the central circular region of the LCOS-SLM surface, the boundaries of the output beams were precisely defined to reduce the extrinsic factors deteriorating the output LG beam quality. Experiments and theoretical analyses were performed for output beams obtained from both Gaussian and top-hat input beams to reveal that the top-hat input beam was more suitable for universally generating higher-order LG beams than the Gaussian input beam. The present approach will be valuable to provide light sources for optical manipulation, optical traps, atom guides, and so on since the LG beam quality affects the trapping and manipulation forces when the LG beam is applied to optical manipulation [23]. The technical limitations of the output LG beam quality in the present scheme were considered to mainly arise from the density of the pixelated electrodes of the LCOS-SLM, particularly when generating LG beams of larger mode indices; in this case, the holographic phase pattern became fine and included many flyback regions [22], i.e., jumps of phase value from 0 to 2π; hence the displayed phase pattern deviated from the ideal one to cause the deterioration of the output LG beam quality.

ACKNOWLEDGMENTS

The authors are grateful to T. Hiruma, Y. Suzuki, and Y. Mizobuchi for their encouragement throughout this paper as well as to H. Toyoda and N. Mukohzaka for their helpful discussions.

REFERENCES

1. H. Kogelnik and T. Li, "Laser beams and resonators," Proc. IEEE **54**, 1312–1329 (1966).
2. L. Allen, M. W. Beijersbergen, R. J. C. Spreeuw, and J. P. Woerdman, "Orbital angular momentum of light and the transformation of Laguerre–Gaussian laser modes," Phys. Rev. A **45**, 8185–8189 (1992).
3. L. Allen, "Introduction to the atoms and angular momentum of light special issue," J. Opt. B: Quantum Semiclassical Opt. **4**, S1–S6 (2002).
4. L. Allen, S. M. Barnett, and M. J. Padgett, *Optical Angular Momentum* (IOP Publishing, 2003).
5. D. G. Grier, "A revolution in optical manipulation," Nature **424**, 810–816 (2003).
6. D. G. Grier and Y. Roichman, "Holographic optical trapping," Appl. Opt. **45**, 880–887 (2006).
7. M. W. Beijersbergen, L. Allen, H. E. L. O. van der Veen, and J. P. Woerdman, "Astigmatic laser mode converters and transfer of orbital angular momentum," Opt. Commun. **96**, 123–132 (1993).
8. M. Padgett, J. Arlt, N. Simpson, and L. Allen, "An experiment to observe the intensity and phase structure of Laguerre–Gaussian laser modes," Am. J. Phys. **64**, 77–82 (1996).
9. J. Courtial, K. Dholakia, L. Allen, and M. J. Padgett, "Second-harmonic generation and the conservation of orbital angular momentum with high-order Laguerre–Gaussian modes," Phys. Rev. A **56**, 4193–4196 (1997).
10. M. A. Golub, E. L. Kaganov, A. A. Kondorov, V. A. Soĭfer, and G. V. Usplen'ev, "Experimental investigation of a multibeam holographic optical element matched to Gauss–Laguerre modes," Sov. J. Quantum Electron. **26**, 184–186 (1996) [Kvantovaya Elektron. (Moscow) **23**, 188–190 (1996)].
11. J. Arlt, K. Dholakia, L. Allen, and M. J. Padgett, "The production of multiringed Laguerre–Gaussian modes by computer-generated holograms," J. Mod. Opt. **45**, 1231–1237 (1998).
12. S. N. Khonina, V. V. Kotlyar, V. A. Soifer, P. Pääkkönen, J. Simonen, and J. Turunen, "An analysis of the angular momentum of a light field in terms of angular harmonics," J. Mod. Opt. **48**, 1543–1557 (2001).
13. S. A. Kennedy, M. J. Szabo, H. Teslow, J. Z. Porterfield, and E. R. I. Abraham, "Creation of Laguerre–Gaussian laser modes using diffractive optics," Phys. Rev. A **66**, 043801 (2002).
14. V. V. Kotlyar, S. N. Khonina, A. A. Almazov, V. A. Soifer, K. Jefimovs, and J. Turunen, "Elliptic Laguerre–Gaussian beams," J. Opt. Soc. Am. A **23**, 43–56 (2006).
15. J. Arlt, T. Hitomi, and K. Dholakia, "Atom guiding along Laguerre–Gaussian and Bessel light beams," Appl. Phys. B **71**, 549–554 (2000).
16. J. E. Curtis, B. A. Koss, and D. G. Grier, "Dynamic holographic optical tweezers," Opt. Commun. **207**, 169–175 (2002).
17. R. Agarwal, K. Ladavac, Y. Roichman, G. Yu, C. M. Liever, and D. G. Grier, "Manipulation and assembly of nanowires with holographic optical traps," Opt. Express **13**, 8906–8912 (2005).
18. A. Lafong, W. J. Hossack, J. Arlt, T. J. Nowakowski, and N. D. Read, "Time-multiplexed Laguerre–Gaussian holographic optical tweezers for biological applications," Opt. Express **14**, 3065–3072 (2006).
19. A. Jesacher, S. Fürhapter, C. Maurer, S. Bernet, and M. Ritsch-Marte, "Holographic optical tweezers for object manipulations at an air–liquid surface," Opt. Express **14**, 6342–6352 (2006).
20. Y. Ohtake, T. Ando, N. Fukuchi, N. Matsumoto, H. Ito, and T. Hara, "Universal generation of higher-order multiringed Laguerre–Gaussian beams by using a spatial light modulator," Opt. Lett. **32**, 1411–1413 (2007).
21. T. Inoue, H. Tanaka, N. Fukuchi, M. Takumi, N. Matsumoto, T. Hara, N. Yoshida, Y. Igasaki, and Y. Kobayashi, "LCOS spatial light modulator controlled by 12-bit signals for optical phase-only modulation," Proc. SPIE **6487**, 64870Y (2007).
22. X. Wang, B. Wang, P. J. Bos, J. E. Anderson, J. J. Pouch, and F. A. Miranda, "Finite-difference time-domain simulation of liquid-crystal optical phased array," J. Opt. Soc. Am. A **22**, 346–354 (2005).
23. A. Jesacher, A. Schwaighofer, S. Fürhapter, C. Maurer, S. Banet, and M. Ritsch-Marte, "Wavefront correction of spatial light modulators using an optical vortex image," Opt. Express **15**, 5801–5808 (2007).
24. X. Xun and R. W. Cohn, "Phase calibration of spatially nonuniform spatial light modulators," Appl. Opt. **43**, 6400–6406 (2004).
25. J. Harriman, A. Linneberger, and S. A. Serati, "Improving spatial light modulator performance through phase compensation," Proc. SPIE **5553**, 58–67 (2004).
26. J. D. Schmidt, M. E. Goda, and B. D. Duncan, "Aberration production using a high-resolution liquid-crystal spatial light modulator," Appl. Opt. **46**, 2423–2433 (2006).
27. G. Machavariani, N. Davidson, E. Hasman, S. Blit, A. A. Ishaaya, and A. A. Friesem, "Efficient conversion of a Gaussian beam to a high purity helical beam," Opt. Commun. **209**, 265–271 (2002).
28. M. A. Clifford, J. Arlt, J. Courtial, and K. Dholakia, "High-order Laguerre–Gaussian laser modes for studies of cold atoms," Opt. Commun. **156**, 300–306 (1998).